1996-06-01

Observed and simulated northern hemisphere intraseasonal circulation anomalies and the influence of model bias

Reynolds, C.; Gelaro, R.; Murphree, T.

American Meteorological Society

Journal Name: Monthly Weather Review; Journal Volume: 124; Journal Issue: 6;
Other Information: PBD: Jun 1996
http://hdl.handle.net/10945/60984

Observed and Simulated Northern Hemisphere Intraseasonal Circulation Anomalies and the Influence of Model Bias

CAROLYN REYNOLDS AND RONALD GELARO

Naval Research Laboratory, Monterey, California

TOM MURPHREE

Department of Meteorology, Naval Postgraduate School, Monterey, California

(Manuscript received 14 August 1995, in final form 11 December 1995)

ABSTRACT

The ability of an atmospheric general circulation model to simulate the observed primary modes of intraseasonal variability in the Northern Hemisphere upper-tropospheric winds during boreal winter is examined. The model used is the Navy Operational Global Atmospheric Prediction System. The authors examine differences between the observed and modeled modes of variability in the context of various model deficiencies, where the observed modes are derived from the European Centre for Medium-Range Weather Forecasts analyses. Rotated empirical orthogonal function analysis is used to determine the primary modes of variability in the Pacific and Atlantic regions. EOFs are computed for both the zonal and meridional wind components. Time-lagged composite analysis is used to examine the temporal evolution of these modes, as well as their relationship to tropical convection. Wave activity flux vectors are used to examine further the characteristics of these intraseasonal modes and their relationship to tropical and extratropical forcing.

It is found that the model simulates the extratropically forced modes well but simulates modes associated with tropical heating poorly. The poor tropical simulation is due primarily to the model's poor representation of the Madden–Julian oscillation (MJO). The model's inability to produce the MJO-related modes is reflected in the model upper-tropospheric wind field variability being too weak in the tropical and subtropical Indian and Pacific Ocean regions. Model biases in the simulated time-mean winds may also account for differences between the observed and modeled modes of variability.

1. Introduction

Many studies have shown that observed intraseasonal variations in tropical convection are related to extratropical circulation anomalies and that the characteristics of the extratropical anomalies may be significantly affected by aspects of the time-mean flow. Therefore, it is natural to assume that model deficiencies in tropical convection and/or the time-mean circulation will have an impact on the model simulation of extratropical intraseasonal circulation anomalies. In this study we compare the primary modes of Northern Hemisphere wintertime intraseasonal variability in observations with those in a 10-yr integration of a general circulation model (GCM) and assess how model deficiencies may impact the simulated modes.

Various relationships between the Madden–Julian oscillation (MJO; Madden and Julian 1972), particularly the eastward-propagating outgoing longwave radiation (OLR) anomalies associated with it, and extratropical circulation anomalies have been established (e.g., Liebmann and Hartmann 1984; Lau and Phillips 1986; Knutson and Weickmann 1987; Livezey and Mo 1987; Kushnir and Wallace 1989; Schubert and Park 1991; Kiladis and Weickmann 1992a; Mo and Kousky 1993). At the same time, many studies have shown that many models produce MJOs with erroneously weak amplitudes and rapid phase speeds compared with those observed (e.g., Lau and Lau 1986; Chen and Alpert 1990; Park et al. 1990; Slingo and Madden 1991). Slingo et al. (1995), in a comparison of 15 different GCMs, found that the best simulations of the MJO occur in models with realistic time-mean precipitation fields. Midlatitude intraseasonal variability has also been found to be weaker than observed in GCMs (Lau and Nath 1987). Schubert et al. (1993) attribute one-third of a GCM's missing intraseasonal variability in the extratropical upper-tropospheric zonal wind field over the Pacific to its weak simulation of the MJO. The deficiencies in GCM simulations of the MJO are significant given that studies have suggested that there may be greater extratropical medium-range predictability during periods when the

Corresponding author address: Dr. Carolyn Reynolds, Naval Research Laboratory, 7 Grace Hopper Avenue, Stop 2, Monterey, CA 93943-5502.
E-mail: reynolds@nrlmry.navy.mil

MJO is strong and well simulated (Ferranti et al. 1990; Lau and Chang 1992).

Much theoretical work has also been done to investigate the impact of the mean state on waveguiding and the interactions between the Tropics and extratropics (e.g., Held 1982). It has been proposed that the existence of critical latitudes inhibit the meridional propagation of Rossby waves (Charney 1969; Lau and Lim 1984), that the relatively small gradients of potential vorticity on the flanks of jets act as regions of wave reflection (Branstator 1983), and that the upper-tropospheric westerlies act as ducts for enhanced tropical–extratropical interaction (Webster and Holton 1982; Zhang and Webster 1989). In addition, there have been many observational studies on the influence of the mean flow on transient behavior (Schubert and Park 1991; Kiladis and Weickmann 1992b; Tomas and Webster 1994). It is probable that biases in the model time-mean structure may have a pronounced affect upon the model simulation of transients.

The specific purpose of this study is to compare observed modes of extratropical variability with those in an extended integration of a GCM and to determine how specific model biases may lead to differences in the generation and propagation of these modes. The GCM used is a reduced-resolution version of the global atmospheric model of the Navy Operational Global Atmospheric Prediction System (NOGAPS) (Hogan and Rosmond 1991; Hogan and Brody 1993). We are interested in assessing the model's ability to simulate the primary modes of observed intraseasonal variability in general, not just those modes associated with tropical heating. Thus, we first identify the primary modes of variability in the upper-tropospheric circulation and then examine possible relationships with precipitation and divergence rather than approach the problem by first examining the tropical heating. The method employed is similar to that used by Schubert et al. (1993) to evaluate the National Aeronautics and Space Administration Goddard Laboratory for Atmospheres Aries GCM. However, while they examined the zonal wind variability over the entire Pacific region, we examine both the meridional and zonal wind variability over both the North Pacific and North Atlantic.

The paper is organized as follows. In section 2 we describe the data used for this study. In section 3 we outline our method of analysis. In section 4 we describe the difference between mean and variance fields for the model and observations. In section 5 we present the results from the EOF and composite analyses. Finally, in section 6 we conclude with a discussion of the results.

2. Data

To represent observed upper-level wind fields, we use twice-daily uninitialized analyses (averaged to daily means) from the European Centre for Medium-Range Weather Forecasts (ECMWF) for the eight winter seasons from 1985/86 through 1992/93. To help mitigate the problem of uncertainty in these data, we use only data after November 1985, since the ECMWF analyses before this time were shown to have a poor representation of the tropical divergent wind field (Trenberth and Olson 1988). Of course, it should be noted that a significant amount of uncertainty in the analyzed tropical divergent wind field after this time may still exist (Sardeshmukh and Liebmann 1993).

Microwave Sounding Unit (MSU)–derived daily averaged precipitation estimates (Spencer 1993) are used to represent observed precipitation values over the ocean. Spencer (1993) demonstrates that while there are significant discrepancies between MSU and global precipitation index monthly mean precipitation values, the pentad variability between the two indices is in good agreement.

The model data come from nine winters of a 10-yr integration of NOGAPS run at T47 horizontal resolution (which corresponds to a 2.5° gridpoint resolution), beginning with initial conditions from 1 January 1979. This 10-yr simulation is part of the Atmospheric Model Intercomparison Project (AMIP) sponsored by the World Climate Research Programme and the U.S. Department of Energy. Prescribed time-varying sea surface temperatures (SSTs) were used based on the observed monthly mean fields linearly interpolated to the forecast time. For this study, in the interest of obtaining a larger sample size, winter corresponds to the 6-month period from November through April.

3. Methods

Empirical orthogonal function (EOF) analysis was used to identify the primary modes of variability in the 200-mb winds. EOFs were computed for two regions based on the correlation matrix of the 200-mb zonal (U) and meridional (V) wind fields filtered to retain only variations with periods between 20 and 70 days. This broad band was chosen so as not to exclude a simulated MJO with an erroneously fast or slow phase speed. The filter used is a recursive symmetric band-passed filter described in Kaylor (1977). The first region, which we refer to as the Pacific region, has longitudinal boundaries at 100°E and 80°W, and latitudinal boundaries at 0° and 70°N. The second region, which we refer to as the Atlantic region, has longitudinal boundaries of 120°W and 50°E, and latitudinal boundaries at 0° and 70°N. The regions were chosen to include the areas around and downstream of the east Asian–North Pacific and North Atlantic midlatitude jets. The modes calculated from the observed U and V fields over the Pacific (P) region are referred to as $U\mathrm{P}n_{\mathrm{O}}$ and $V\mathrm{P}n_{\mathrm{O}}$, respectively, where n indicates the EOF (eigenvalue) index and the subscript O refers to the observations. The modes calculated from the model simulation over the Pacific region are denoted by $U\mathrm{P}n_{\mathrm{M}}$

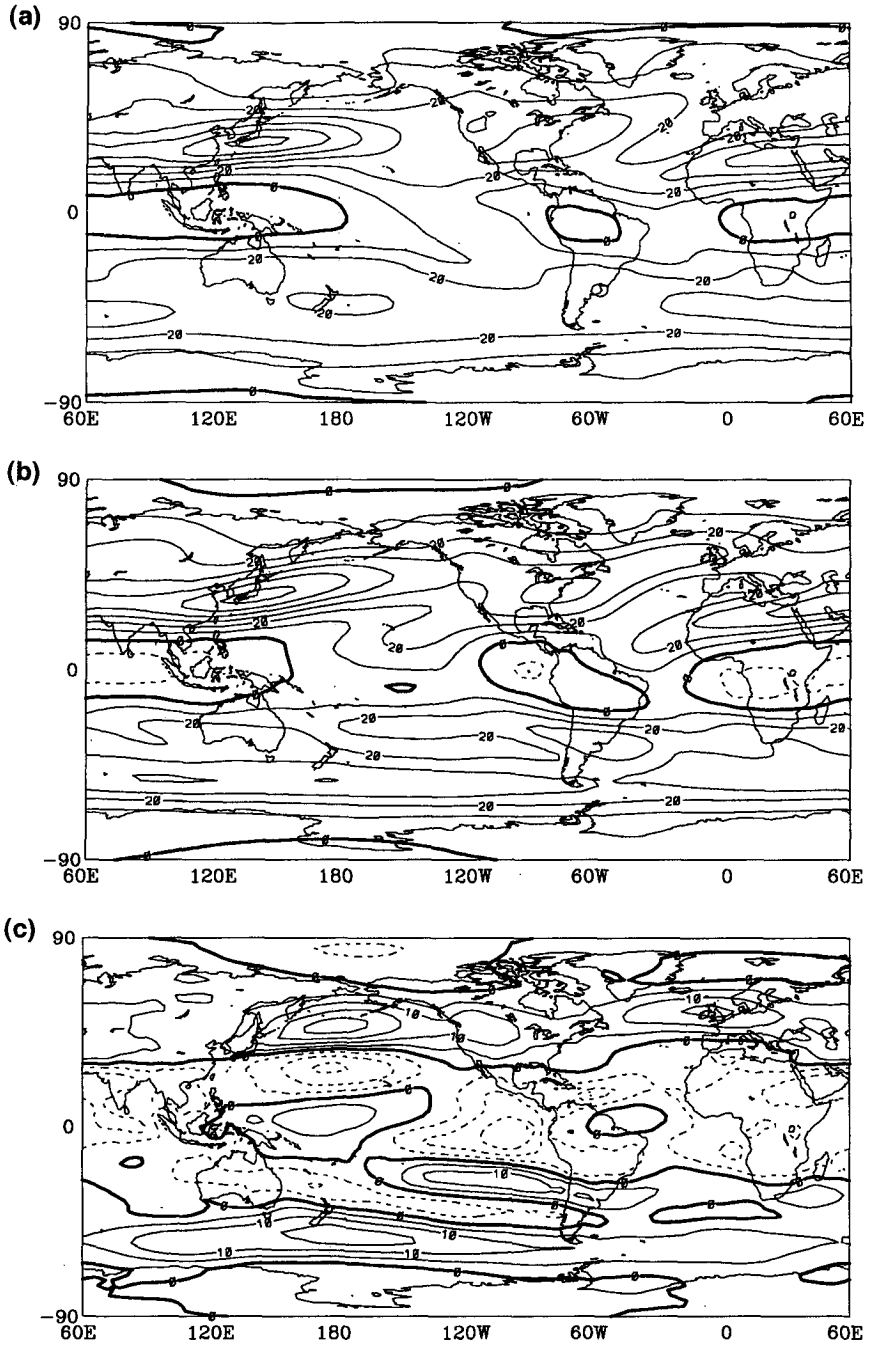

FIG. 1. The 200-mb U November through April climatology for (a) observations and (b) model simulation. The model bias (model minus observations) is shown in (c). Contour interval in (a) and (b) is 10 m s^{-1}. Contour interval in (c) is 5 m s^{-1}. Negative contours are dashed.

and VPn_M, where the subscript M refers to the model. Likewise, the modes calculated over the Atlantic (A) region are denoted by UAn_O, VAn_O, etc.

The 2.5° model gridpoint data were interpolated to an equal-area grid with horizontal resolution ranging from 2.5° at the equator to 5° at 60°N. This results in 1630 grid points in the Pacific region and 1530 grid points over the Atlantic region. The EOFs were orthogonally rotated using the Varimax method in order to decrease the sensitivity of the EOFs to sampling errors (Richman 1986; Barnston and Livezey 1987). The number of modes retained was determined by exami-

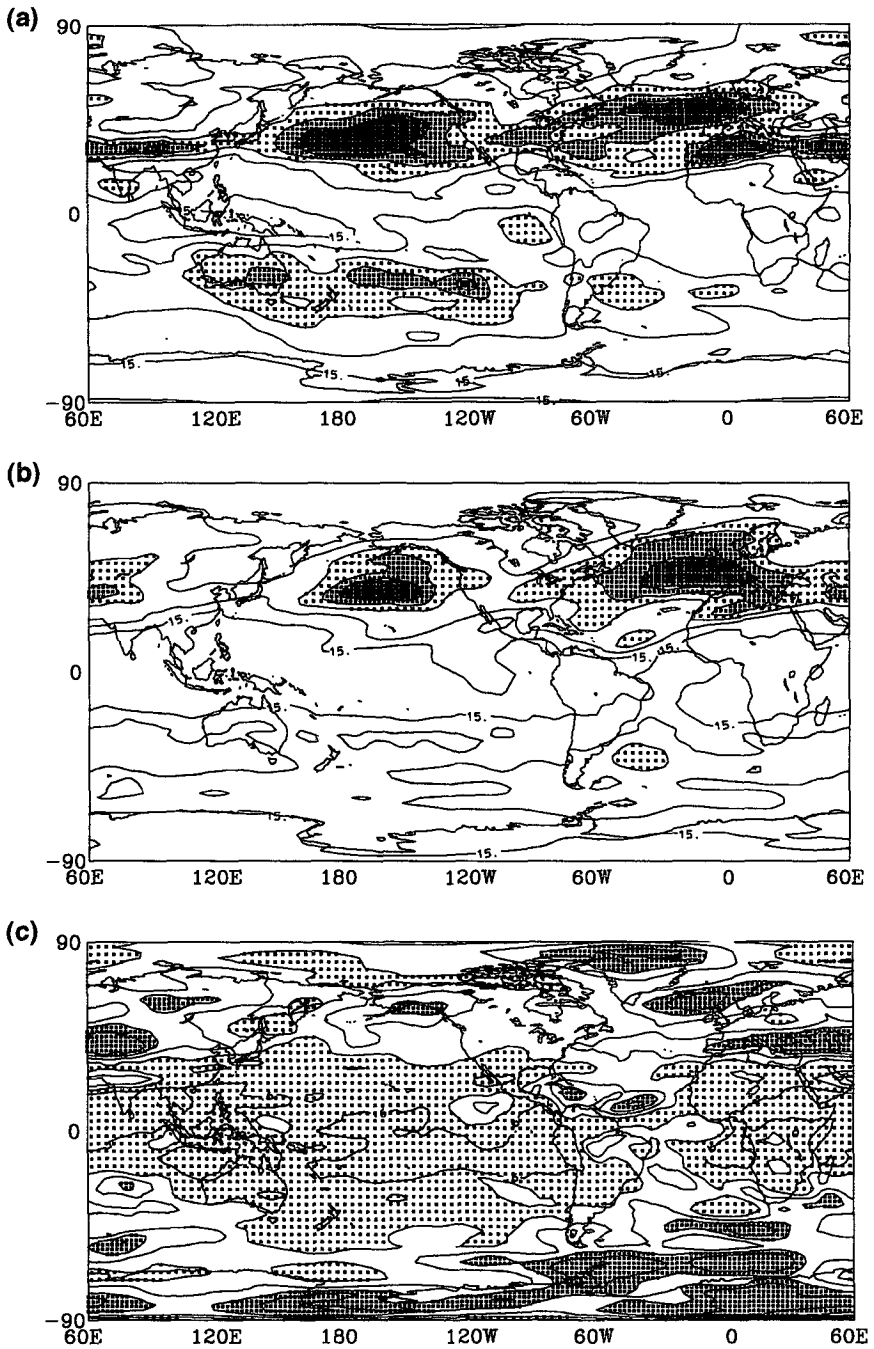

FIG. 2. The 20–70-day winter variance for the 200-mb U field for (a) observations and (b) model simulation. The percent difference between the two [(model − observations)/observations] is shown in (c). The contour interval in (a) and (b) is 15 $m^2 s^{-2}$, and values greater than 45 $m^2 s^{-2}$ are shaded. The contour interval in (c) is 30%, with dark (light) shading indicating regions greater than 30% (less than −30%).

nation of the eigenvalues (O'Lenic and Livezey 1988). None of the remaining modes excluded from the rotation represented independent eigenvectors (North et al. 1982). The number of modes retained ranged from 5 to 8. The rotated modes presented in this study were found to be relatively insensitive to retaining one less or one more mode and, in most cases, were qualitatively similar to the nonrotated modes.

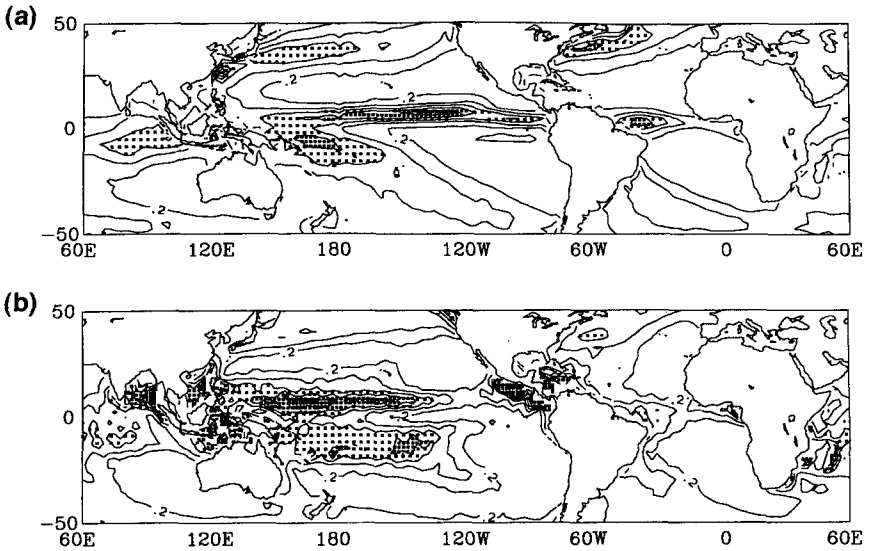

FIG. 3. Mean winter precipitation rate climatology over the ocean for (a) MSU-derived observations and (b) model simulation. The contour interval is 0.2 cm day^{-1} with values greater than 0.6 cm day^{-1} shaded.

Composites were calculated by averaging a particular field, such as the 200-mb streamfunction, over all the days that corresponded to a relative maximum or minimum value of the principal components for a particular EOF. The principal components are the temporal amplitudes that correspond to the spatial patterns represented by the EOFs. Only maxima and minima within the top and bottom 25% of all principal component values were included. A maximum (minimum) with a larger (smaller) value within 5 days was not included in the composite. Lagged composites were similarly calculated by averaging fields corresponding to a specific number of days before or after the maxima and minima. *Maximum (minimum) anomalies* were computed by subtracting the time-mean winter climatology from the composites based on the maxima (minima) of the principal components. *Difference anomalies* were formed by subtracting the composites based

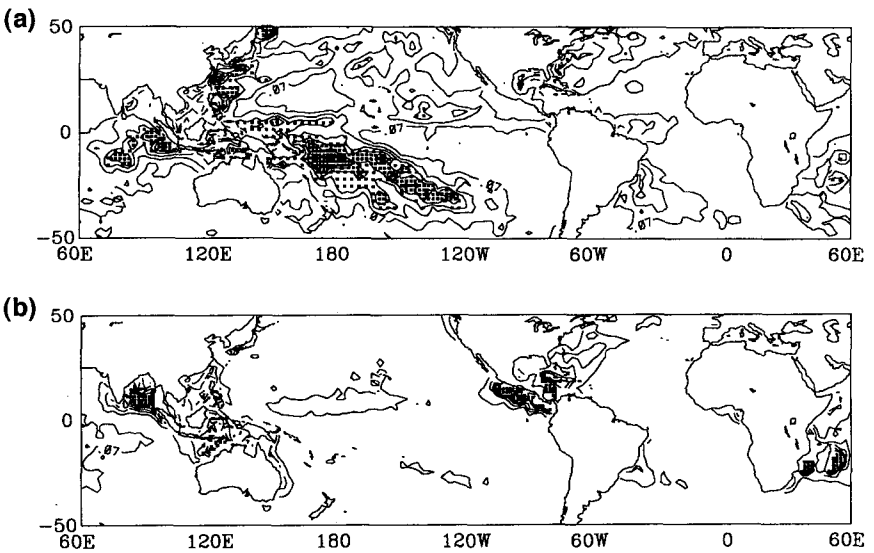

FIG. 4. The 20–70-day winter variance for ocean precipitation for (a) observations and (b) model simulation. The contour interval is 0.07 cm^2 day^{-2} with values greater than 0.21 cm^2 day^{-2} shaded.

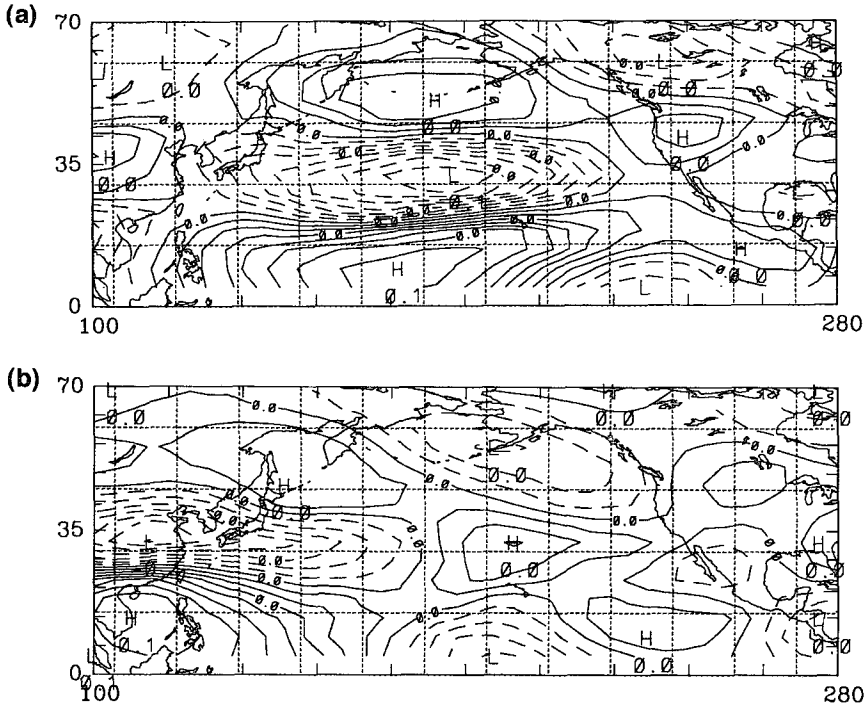

FIG. 5. The (a) first and (b) second eigenvectors based on the observed 200-mb U field over the Pacific region. Units are nondimensional.

on the minima from the composites based on the maxima. There were approximately four maxima and minima per season, or between 30 and 40 dates in each composite. The significance of the anomalies was estimated based on 100 composites of randomly chosen dates with sample sizes of 32 and 36 for the observed and modeled data, respectively.

The technique described above is similar to that employed by Schubert et al. (1993) but with some important differences. First, in order to focus exclusively on Northern Hemisphere variability, we do not include the Southern Hemisphere extratropics when calculating the EOFs. Second, we examine both Pacific and Atlantic modes of variability. Third, we calculate EOFs based on both U and V fields because they highlight different aspects of certain phenomena.

4. Mean and variance fields

To evaluate the differences between the observed and modeled modes of variability in the context of model biases, we first examine the observed and modeled mean and variance fields of the 200-mb U and precipitation fields. The observed and modeled 200-mb U fields are shown in Fig. 1. The model captures the basic features of the Northern Hemisphere extratropics. The midlatitude jets are fairly well simulated, although the jets are positioned slightly poleward of their observed locations and are too strong over the central North Pacific and North Atlantic. The model also captures the two regions of upper-tropospheric westerlies in the Tropics, although the magnitude of the westerlies is smaller than observed. In the Southern Hemisphere, the model produces a much stronger jet than observed at 50°S over the South Pacific, while underestimating wind speeds over Australia. Figure 1c shows the difference between the two fields (model bias). This figure clearly shows the poleward shift of the simulated Northern Hemisphere midlatitude jets, especially in the North Pacific and North Atlantic. Also apparent is the model's easterly bias throughout the Tropics and subtropical Northern Hemisphere, with the exception of the two regions over the tropical western Pacific and Atlantic.

Figure 2 shows the observed and modeled 20–70-day variance of the 200-mb U field. The locations of the two major observed maxima (Fig. 2a) over the North Pacific and North Atlantic are well simulated by the model (Fig. 2b), although the magnitudes are smaller than observed. The percent difference between the two fields (Fig. 2c) shows that the magnitude of the modeled variance is within 30% of the observed variance over much of the extratropics poleward of 30°N, and greater than 30% too strong in some isolated regions. The variance over most of the Tropics and subtropics from Africa eastward to the eastern Pacific is seriously underestimated ($< -30\%$). However, the tropical and subtropical

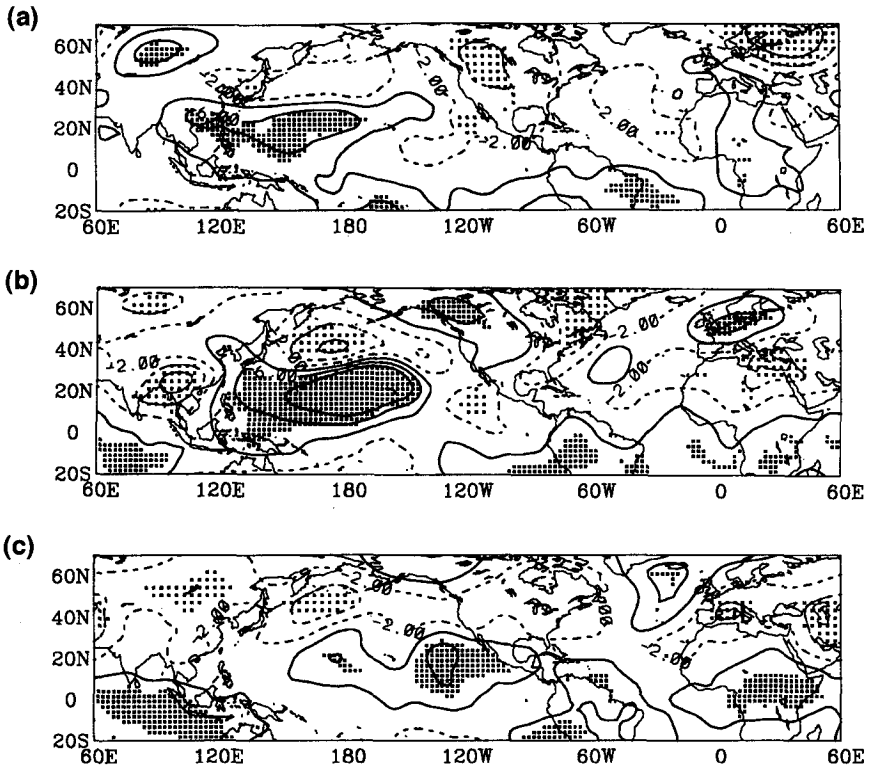

FIG. 6. The 200-mb streamfunction minimum anomalies for $UP1_O$ at (a) lag −8 days, (b) lag +0 days, and (c) lag +8 days. Contours at ±2, ±6, and ±10 × 10^6 m^2 s^{-1} with positive (negative) values significant at the 99% level indicated by dark (light) shading. Negative contours are dashed.

variance is better simulated over the Americas and the Atlantic and is even too strong in some areas of this region. Similar bias patterns are found for the 200-mb *V* field variance (not shown).

The average winter precipitation over the ocean, as determined from MSU-derived estimates and from the model simulation, are shown in Fig. 3. The global-scale precipitation features are fairly well simulated by NOGAPS, but there are errors in both intensity and position. The modeled intertropical convergence zone (ITCZ) is too strong in the western Pacific, and the South Pacific convergence zone (SPCZ) does not extend southeastward into the central South Pacific as observed. There are isolated areas of excessive rainfall, primarily over the Bay of Bengal and the areas around Madagascar and central America. Midlatitude storm tracks are evident but are weaker than observed. It should be noted, however, that the MSU storm-track precipitation may be overestimated (Spencer 1993).

Figure 4 shows the 20–70-day variability of the MSU-derived precipitation and modeled precipitation. The region of largest observed variance extends eastward from the eastern Indian Ocean into the central Pacific and is especially strong in the SPCZ (Fig. 4a). These are the areas where the observed MJO has the largest signal in tropical heating (e.g., Knutson and Weickmann 1987). In contrast, the modeled 20–70-day variance is severely underestimated in the western and central Pacific, even though the model produces adequate amounts of precipitation in these areas in a time-mean sense (Fig. 3b). There are only a few regions where the modeled 20–70-day variability is larger than observed, and they reflect the highly localized biases in the mean precipitation fields described above.

This lack of intraseasonal variability suggests that the model does not adequately simulate the MJO. Hovmöller diagrams of the simulated 200-mb velocity potential (not shown) reveal an eastward-propagating wavenumber 1 signal indicative of the MJO but with much weaker amplitude than observed, especially in the Eastern Hemisphere. These results appear to confirm that the model does a poor job of simulating the MJO.

5. EOF analysis

a. Pacific U

Figure 5 shows the two leading modes of the eight rotated EOFs for the observed 200-mb *U* field over the Pacific region ($UP1_O$ and $UP2_O$). Together, these modes represent 23% of the 20–70-day variance in this

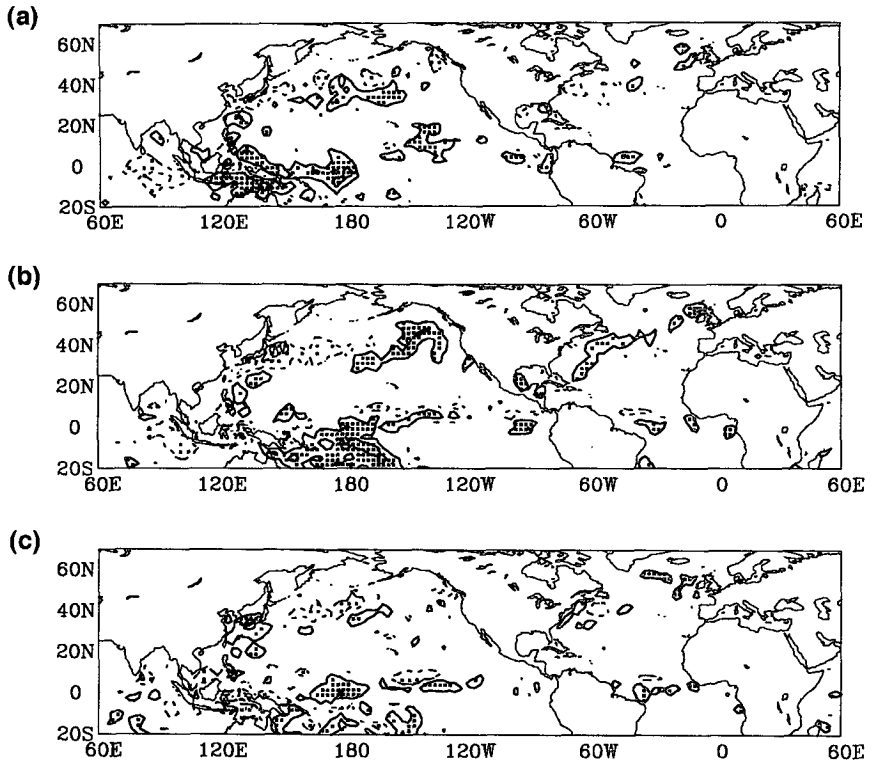

FIG. 7. The precipitation minimum anomalies for $UP1_O$ at (a) lag -8 days, (b) lag $+0$ days, and (c) lag $+8$ days. Contours at ± 0.2, ± 0.6, and ± 1.0 cm day^{-1} with positive (negative) values significant at the 95% level indicated by dark (light) shading. Negative contours are dashed.

region. (The variance referred to here is normalized spatially by the local variance, since we are basing our EOFs on a correlation, rather than covariance, matrix.) The first two modes of the observations are in approximate east–west quadrature with each other, and both show subtropical easterlies (westerlies) associated with tropical westerlies (easterlies) in the central and western Pacific.

Figure 6 shows the 200-mb streamfunction minimum anomaly for $UP1_O$ at time lags of -8, 0, and $+8$ days. Negative (positive) lags precede (follow) the principal component minima. The shading shows areas where the anomalies are significant at the 99% level. These time-lagged composites, as well as composites based on $UP2_O$ (not shown), indicate that these modes represent a subtropical anticyclone that propagates eastward from the Indian Ocean to the region of the date line and then dissipates. Subtropical anticyclones (cyclones) in the west Pacific are accompanied by cyclones (anticyclones) in the Indian Ocean (Fig. 6b). The principal components of $UP1_O$ and $UP2_O$ have a maximum correlation of 0.4 when the former lags the latter by 9 days, suggesting that these two EOFs represent different phases of the same physical phenomenon. Period spectral density plots of the principal components indicate that both EOFs have spectral peaks between 50 and 60 days.

Figure 7 shows the precipitation minimum anomalies corresponding to the same times as in Fig. 6. In the case of precipitation anomalies, shading indicates anomalies significant at the 95% level. One can see an eastward-propagating positive precipitation anomaly that occurs equatorward of the subtropical anticyclonic anomaly (Fig. 6) and dissipates in the central Pacific. A similar relationship is found between subtropical cyclonic anomalies and negative precipitation anomalies composited about the maximum phases of these modes, although the relationship is much weaker and less significant. Time-lagged composites of the 200-mb velocity potential based on both of these modes (not shown) indicate a significant wavenumber 1 pattern that propagates eastward around the globe with a period of approximately 50 days. The eastward-propagating precipitation anomalies and the subtropical anticyclones shown here are very similar to findings in several previous studies of the MJO and its related extratropical circulation anomalies (e.g., Knutson and Weickmann 1987; Schubert and Park 1991).

Time-lagged composites based on the leading EOFs of the model's 200-mb U field over the Pacific region

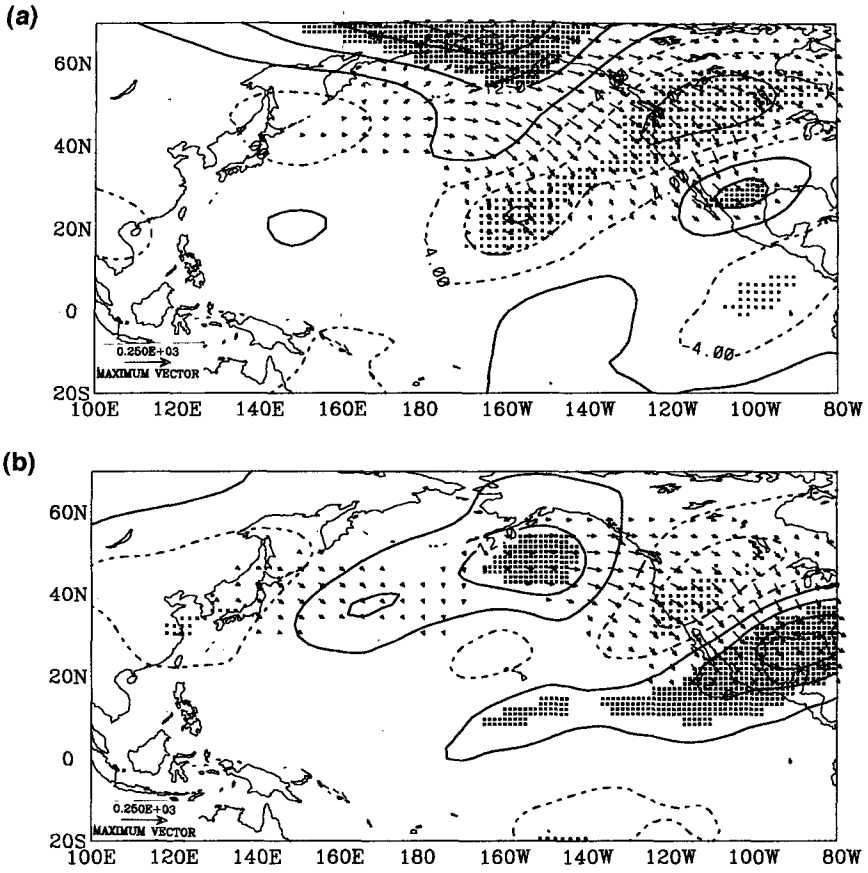

FIG. 8. The 200-mb streamfunction difference anomalies for (a) $UP3_O$ and (b) $UP3_M$. Contours at ± 4, ± 12, and $\pm 20 \times 10^6$ m^2 s^{-1} with positive (negative) values significant at the 99% level indicated by dark (light) shading. Negative contours dashed. The corresponding horizontal wave activity fluxes are represented by the vectors (m^2 s^{-2}).

show no eastward-propagating mode similar to $UP1_O$ or $UP2_O$ and no mode with a significant signal in tropical convection. The significance here is that the model completely fails to reproduce the MJO-related modes that account for 23% of the observed variability in this region. These results suggest that the model's inability to produce an adequate MJO results in significantly decreased simulated variability in the tropical and subtropical wind over the Indian Ocean and western and central Pacific regions (Fig. 2). These results are very similar to those found by Schubert et al. (1993) for the Goddard Aries GCM.

In contrast with the MJO-related modes, both the third and fourth observed modes in the Pacific region ($UP3_O$ and $UP4_O$) are fairly well simulated by the model. Perhaps not surprisingly, these modes show no strong signal in tropical precipitation. Figure 8 shows the 200-mb streamfunction difference anomalies for $UP3_O$ and its model counterpart $UP3_M$. The stationary wave activity flux vectors for these difference anomalies are also shown in Fig. 8. The horizontal components of the stationary wave activity flux **F** were computed following Plumb (1985); that is,

$$F_u = p\cos\phi\left[v'^2 - \frac{1}{2\Omega a \sin 2\phi}\frac{\partial(v'\Phi')}{\partial\lambda}\right]$$

$$F_v = p\cos\phi\left[-u'v' + \frac{1}{2\Omega a \sin 2\phi}\frac{\partial(u'\Phi')}{\partial\lambda}\right],$$

where u', v', and Φ' are the zonally asymmetric parts of the difference anomaly 200-mb geostrophic wind components and geopotential fields, respectively; p is the pressure ratio, 200 mb/1000 mb; Ω is the earth's rotation rate; a is the earth's radius; ϕ is latitude; and λ is longitude. The flux vectors indicate the horizontal direction and strength of stationary wave energy propagation. The divergence and convergence of these vectors indicate wave energy source and sink regions, respectively. The streamfunction difference anomaly based on $UP3_O$ (Fig. 8a) is similar to $UP3_M$ (Fig. 8b). Both the observed and modeled anomalies and flux

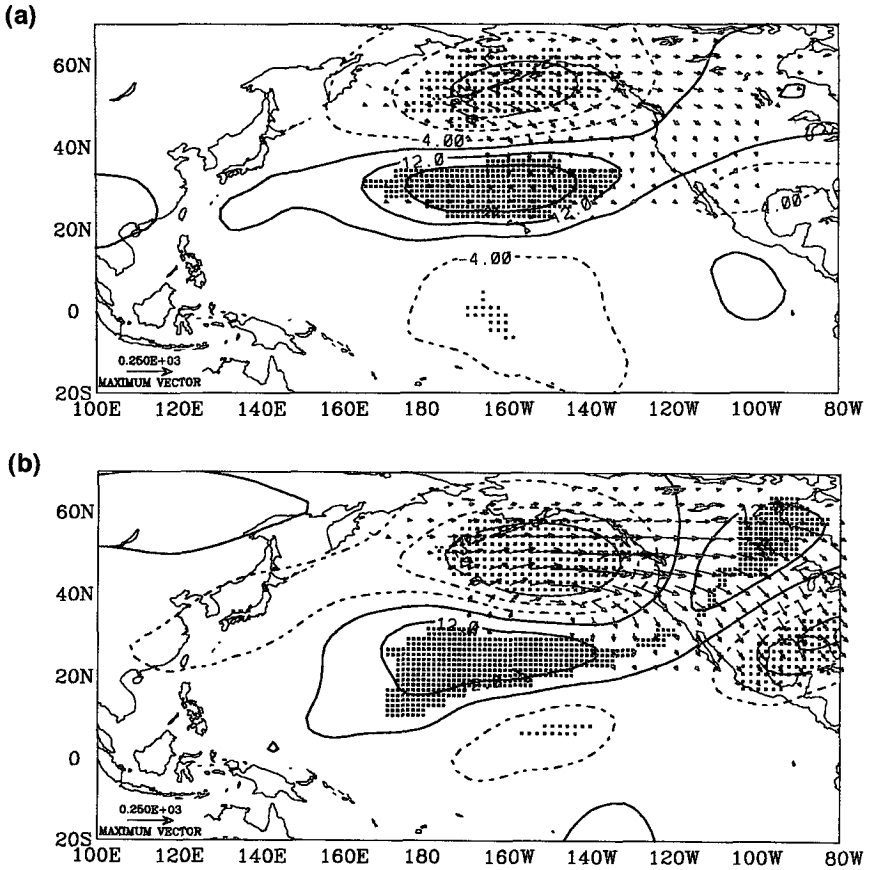

FIG. 9. The 200-mb streamfunction difference anomalies for (a) $UP4_O$ and (b) $UP2_M$. Contours at ± 4, ± 12, and $\pm 20 \times 10^6$ m^2 s^{-1} with positive (negative) values significant at the 99% level indicated by dark (light) shading. Negative contours dashed. The corresponding horizontal wave activity fluxes are represented by the vectors (m^2 s^{-2}).

vectors indicate a wave train emanating from the central North Pacific that extends eastward and southward toward North America. Although the observed wave pattern has far more energy over Alaska, its structure over North America is well simulated by the model. These EOFs represent 7% of the variance in both the observations and the model, and the period spectral density plots of the principal components both have their highest values at around 60 days. The flux vectors indicate extratropical wave energy sources over the North Pacific for both the observed and modeled difference anomalies. The main source region for the observed mode is located southeast of the Kamchatka Peninsula, while the main source region for the simulated mode is located south of the Aleutian Islands. Precipitation difference anomalies based on these EOFs (not shown) are not significant at the 95% level.

Figure 9 shows the 200-mb streamfunction difference anomalies and the wave activity flux vectors based on the fourth observed mode ($UP4_O$; Fig. 9a) and the corresponding mode in the model ($UP2_M$; Fig. 9b). In both cases, the pattern resembles the Pacific–North America (PNA) pattern (Wallace and Gutzler 1981). These EOFs represent 7% and 11% of the observed and modeled variance, respectively, and period spectral density plots of the principal components show highest values between 50 and 70 days. These streamfunction difference anomalies are quite similar to those shown for the PNA mode in Fig. 6 of Schubert et al. (1993). The wave activity flux vectors for both patterns indicate extratropical energy sources over the midlatitude North Pacific with energy propagation eastward and southward across much of the northeast Pacific and North America. Extended Eliassen–Palm fluxes (Hoskins et al. 1983) based on these composites (not shown) indicate a conversion from zonal to eddy kinetic energy in the exit region of the North Pacific jet similar to those found for PNA-type patterns in previous studies (e.g., Simmons et al. 1983; Schubert et al. 1993). The maximum phase of these EOFs represents periods when the east Asian jet has shifted eastward and extends far across the North Pacific, while the minimum phase represents periods when the jet has re-

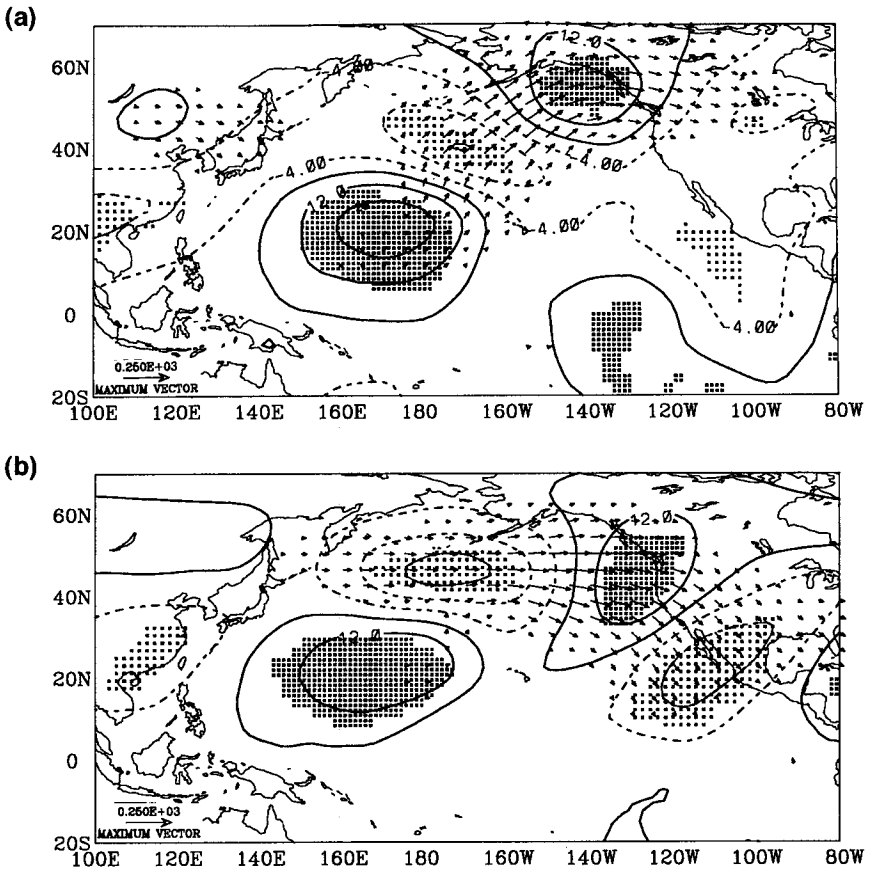

FIG. 10. The 200-mb streamfunction difference anomalies for (a) $VP2_O$ and (b) $VP1_M$. Contours at ±4, ±12, and ±20 × 10^6 m^2 s^{-1} with positive (negative) values significant at the 99% level indicated by dark (light) shading. Negative contours dashed. The corresponding horizontal wave activity fluxes are represented by the vectors (m^2 s^{-2}).

tracted westward over Asia. Difference anomalies for the 200-mb *U* field (not shown) indicate wind speed differences of more than 30 m s^{-1} over the central and eastern North Pacific between the maximum and minimum phases of these modes in both the observations and model.

The precipitation anomalies corresponding to the streamfunction anomalies in Fig. 9 (not shown) indicate that for both the observations and model simulation the extended jet phase is associated with an increase in precipitation over the southern Gulf of Alaska and the northwest coast of North America, although this increase is more substantial for the modeled mode than for the observed mode.

None of the modeled EOFs, and only the first two observed EOFs (Fig. 7), have a significant signal in the tropical precipitation anomalies. The above results indicate that the model fails to reproduce the observed *U* modes that are associated with tropical precipitation but simulates well those modes that are not associated with such heating. The modes that are well simulated are those that appear to be forced by midlatitude processes. These results are consistent with those in Fig. 2 that show that the model poorly simulates the observed tropical and subtropical variability over the Indian and Pacific Oceans but adequately simulates the observed midlatitude variability over the North Pacific and North America.

b. Pacific V

In this section, we examine composites based on the EOFs of the 200-mb *V* field. We focus our attention on two types of patterns common to both the observations and the model simulation. Although the observed and modeled patterns are similar, some differences between them may be explained by particular model biases. The first type of pattern represents a circulation pattern dominated by a subtropical anticyclone over the central Pacific. The second type of pattern represents an east–west-oriented wave train that stretches across the Pacific.

Figure 10 shows the 200-mb streamfunction difference anomalies and the corresponding wave activity

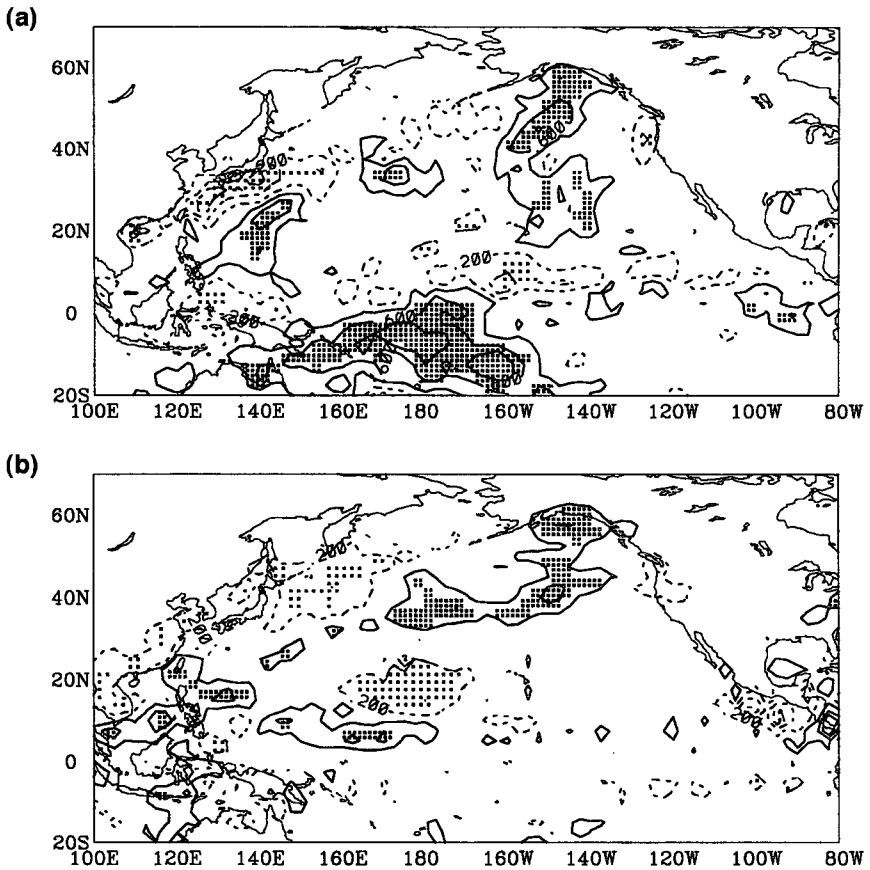

FIG. 11. Same as Fig. 10 but for the precipitation difference anomalies. Contours at ±0.2, ±0.6, and ±1.0 cm day^{-1} with positive (negative) values significant at the 95% level indicated by dark (light) shading. Negative contours are dashed.

flux vectors for the first type of pattern in the observations ($VP2_O$; Fig. 10a) and in the model ($VP1_M$; Fig. 10b). These EOFs represent 10% and 11% of the observed and modeled variance, respectively, and period spectral density plots of the principal components show the highest peaks at around 60 days. Both modes show a prominent subtropical anticyclone near the date line and what appears to be a wave train emanating poleward and eastward from this feature. The observed wave activity flux shows strong divergence, indicating a wave energy source, in the subtropical North Pacific and energy propagation poleward and eastward from there. The major wave energy source in the model is at 40°–55°N in the North Pacific, and the energy propagates eastward and equatorward from there.

Figure 11 shows the precipitation difference anomalies corresponding to the streamfunction anomalies shown in Fig. 10. Both model and observations show positive precipitation difference anomalies in the Gulf of Alaska that roughly coincide with areas of anomalous southerly flow at 200 mb (Fig. 10). The observations ($VP2_O$) (Fig. 11a) show a significant positive precipitation anomaly on the equatorward side of the subtropical anticyclone. The observed wave activity flux vectors show a subtropical wave source north of this precipitation anomaly, as well as a source near Alaska. The location of the precipitation anomaly just south of the subtropical anticyclone and region of wave activity flux divergence is consistent with the wave train being forced, in part, by the tropical heating anomaly, although efforts to verify this through Rossby wave source calculations (Sardeshmukh and Hoskins 1988) do not provide conclusive results. For the model ($VP1_M$) (Fig. 11b), the strong positive precipitation anomaly in the tropical central Pacific and the strong wave energy source in the adjacent northern subtropics are missing. Much of the large difference between the observed and modeled wave activity over the central North Pacific may be due to the model's failure to simulate the tropical Pacific precipitation anomaly.

Correlations between the leading observed U and V modes for the Pacific region indicate a relationship between these modes. The principal components of $VP2_O$ and $UP1_O$ (Fig. 6) have a very strong correlation of

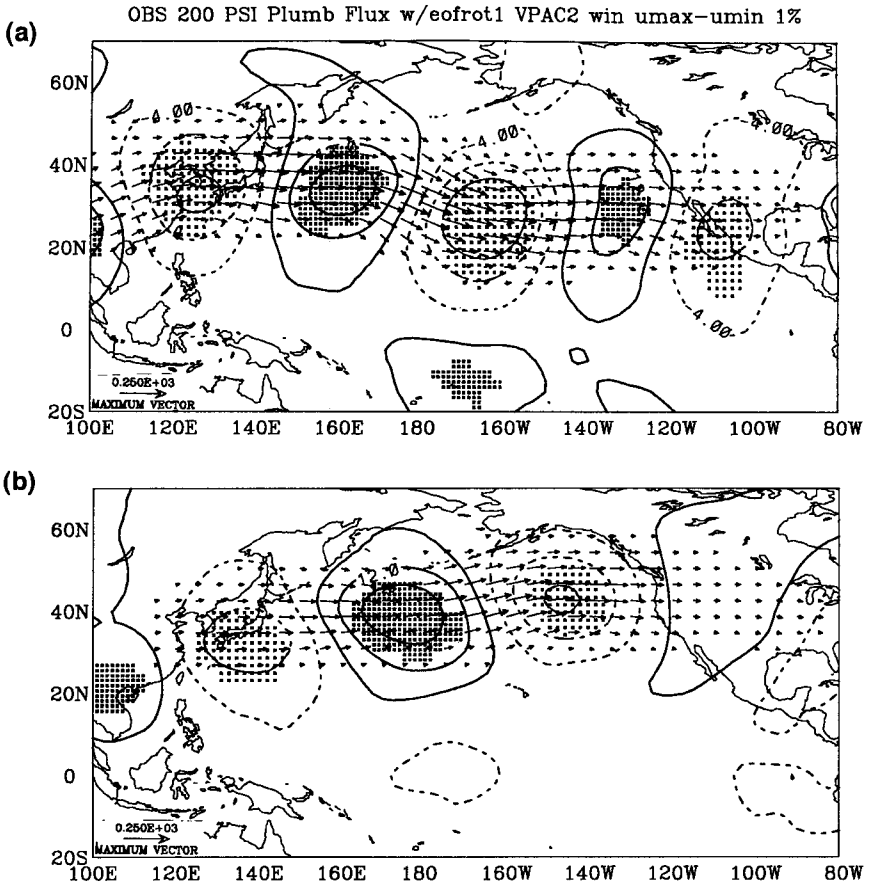

FIG. 12. The 200-mb streamfunction difference anomalies for (a) $VP1_O$ and (b) $VP4_M$. Contours at ± 4, ± 12, and $\pm 20 \times 10^6$ m^2 s^{-1} with positive (negative) values significant at the 99% level indicated by dark (light) shading. Negative contours dashed. The corresponding horizontal wave activity fluxes are represented by the vectors (m^2 s^{-2}).

-0.7 at a lag of $+2$ days. The principal components of $VP2_O$ also have a correlation of -0.4 with the principal components of $UP2_O$ at a lag of $+10$ days. Time-lagged difference anomalies of precipitation and 200-mb velocity potential for $VP2_O$ (not shown) are very similar to those for $UP1_O$ (Fig. 7) and confirm that $VP2_O$ is related to the MJO. While $UP1_O$, $UP2_O$, and $VP2_O$ all appear to be related to the MJO, the U modes emphasize the eastward propagation of the subtropical anticyclone and variations in the midlatitude jet, while the V mode emphasizes the stationary wave fluctuations that occur downstream of the jet over the eastern Pacific and North America. As with the PNA-type mode, the extended Eliassen–Palm fluxes based on these modes (not shown) indicate barotropic energy conversion from the mean flow to the anomalies in the exit region of the jet.

Figure 12 shows the streamfunction difference anomalies and corresponding wave activity flux vectors for the second type of pattern in the observed and simulated modes ($VP1_O$ and $VP4_M$), which represents an east–west-oriented wave train across the Pacific. These EOFs, and the EOFs in quadrature with them, represent 18% and 16% of the observed and modeled variance, respectively. Period spectral density plots of the observed mode indicates a fairly flat spectrum over the entire 20–70-day range, while the modeled mode shows two distinct peaks at 25 and 50 days. Time-lagged difference anomalies indicate that these modes have a very slow eastward propagation speed. The wave trains propagate eastward one wavelength in approximately 35 days. For $VP1_O$ (Fig. 12a), the east–west wave train dips equatorward near the date line and has considerable amplitude at low latitudes. For $VP4_M$ (Fig. 12b), the east–west wave train arcs poleward over the central North Pacific and has little amplitude at low latitudes. These differences may account for some of the model deficiencies in variability in the central and eastern subtropical Pacific (Fig. 2) and may be related to biases in the simulated mean flow.

Figure 13 shows the same wave activity flux vectors shown in Fig. 12 superimposed upon the 200-mb time-

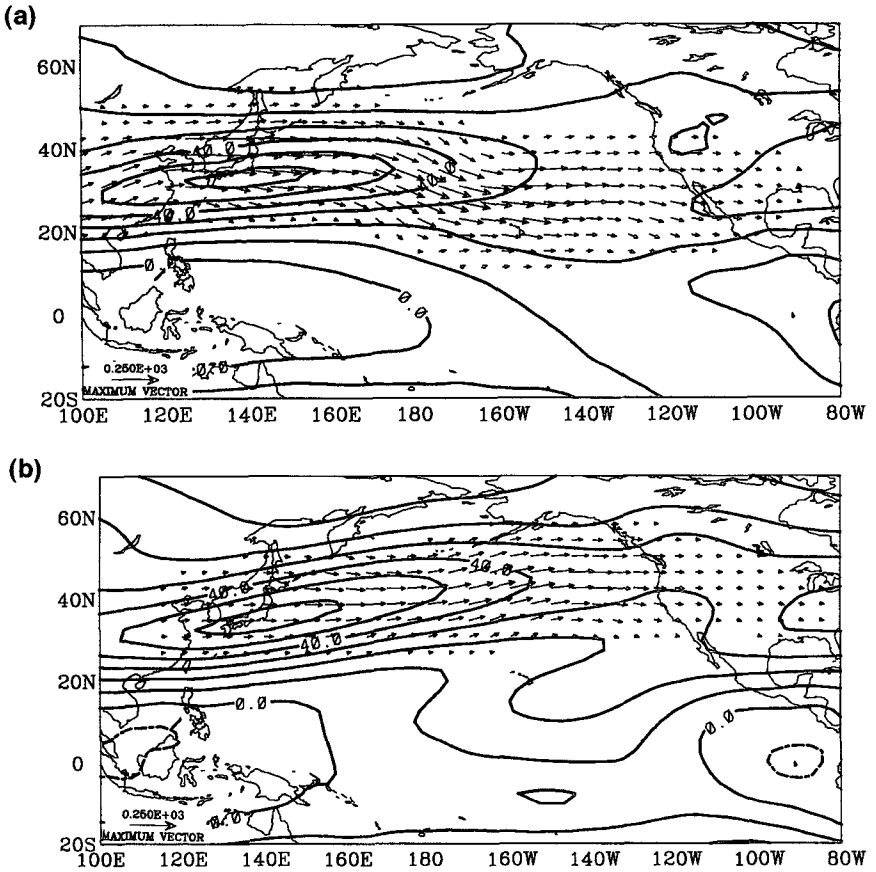

FIG. 13. The same wave activity flux vectors as in Fig. 12, superimposed upon the 200-mb U winter climatology for (a) observations and (b) model simulation. The contour interval is 10 m s^{-1}. Negative contours are dashed.

mean zonal wind. In general, it appears that the flux vectors (and wave trains) are aligned along the jet axis and are bounded on either side by the strong meridional shear zones flanking the jet. However, we see that in the observations (Fig. 13a) the meridional shear on the southern flank of the jet in the central Pacific (180°–160°W), along with the jet itself, is weaker than in the model simulation (Fig. 13b). Where the shear zone weakens, in the exit region of the jet over the central Pacific, the observed wave train shows a strong equatorward component. In contrast, the simulated wave train shows eastward and northward propagation as far as North America. These results are consistent with the findings of Branstator (1983), who suggested that the flanks of the jet act as regions of wave reflection because they are regions where the meridional gradient of potential vorticity goes to zero. These results are also consistent with the findings of Lau and Lim (1984), who show that meridional propagation of stationary waves of zonal wavenumber 5 at 30°N is most efficient at background wind speeds of approximately 20 m s^{-1}.

c. *Atlantic U*

In addition to studying EOFs based on the Pacific region, we have also examined the EOFs for the North Atlantic jet region. The streamfunction and velocity potential anomalies based on the first observed mode ($UA1_O$) (not shown) are very similar to the streamfunction minimum anomaly based on $UP1_O$ (Fig. 6b). In addition, the principal components of this mode have a correlation of −0.5 with the principal components of $UP1_O$ at a lag of −1 day and a correlation of −0.4 with the principal components of $UP2_O$ at a lag of +9 days, suggesting that all three modes are related to the MJO. This mode accounts for 14% of the variance in the Atlantic region, with most of the variance occurring over Africa. This illustrates the dominance of the MJO-related mode not only over the Indian Ocean and Pacific region but also over subtropical Africa. As was the case with the Pacific-based modes, this mode has no counterpart in the model simulation. As in the Pacific, however, the observed modes that show no connection to tropical precipitation or large-scale divergence are well simulated by the model.

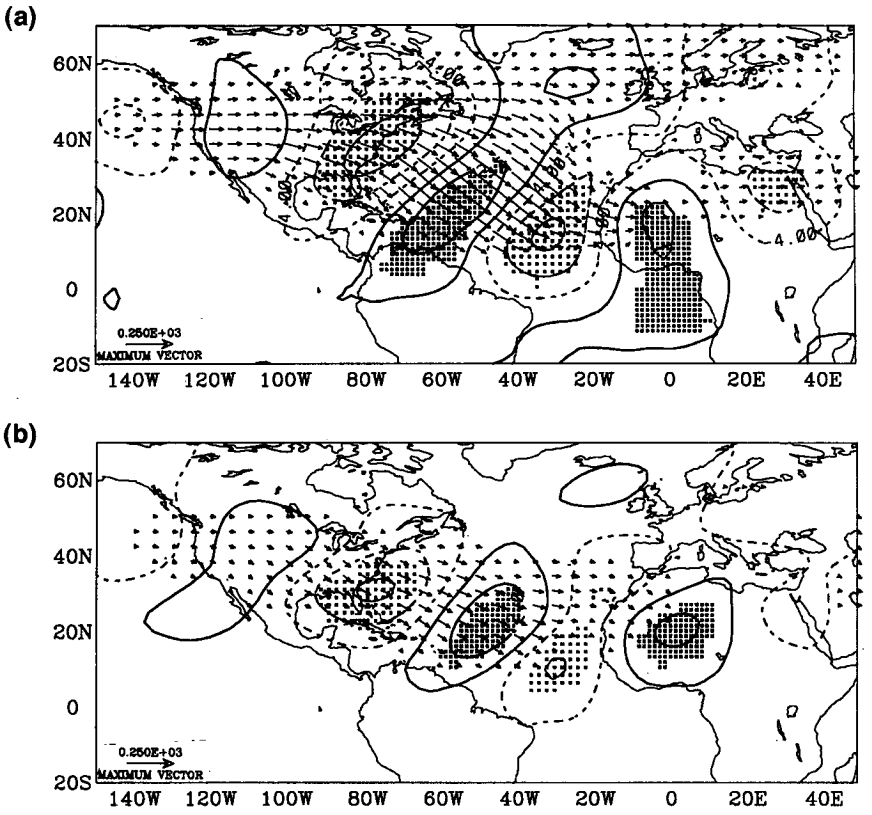

FIG. 14. The 200-mb streamfunction difference anomalies for (a) $VA1_O$ and (b) $VA2_M$. Contours at ± 4, ± 12, and $\pm 20 \times 10^6$ m^2 s^{-1} with positive (negative) values significant at the 99% level indicated by dark (light) shading. Negative contours are dashed. The corresponding horizontal wave activity fluxes are represented by the vectors (m^2 s^{-2}).

The 200-mb streamfunction difference composites and wave activity flux vectors based on the second observed mode ($UA2_O$) and its model counterpart ($UA1_M$) account for 11% and 9% of the observed and modeled variance, respectively. Both observed and modeled modes are very similar to the mode found by Shapiro and Goldenberg (1993), who used rotated principal component analysis to study observed intraseasonal variations in the 200-mb and near-surface U fields over the Atlantic. The modes represent circulation anomalies elongated in the southwest–northeast direction over North America, with neither mode showing a significant signal in tropical precipitation or divergence.

d. Atlantic V

Four of the first five EOFs based on the Atlantic V field represent two types of patterns that are very similar in the observations and the simulation. The first type of pattern is a wave train that arcs over North America southward into the North Atlantic. The second type is a wave train that arcs over the North Atlantic into Europe and Africa. Neither pattern shows any significant relationship to tropical precipitation. Consistent with the results presented above, the model simulates these modes well.

The first pattern is shown in Fig. 14, where the 200-mb streamfunction difference anomalies and corresponding wave activity flux vectors for the first observed ($VA1_O$) and second modeled ($VA2_M$) EOFs of the Atlantic V field are displayed. Both EOFs represent a wave train propagating southeastward across North America and over the Atlantic. For both modes, the wave activity flux vectors indicate wave sources over the northeast Pacific and North America. These modes, and the modes in quadrature with them, represent 20% and 19% of the observed and modeled V field intraseasonal variance in this region, respectively. Period spectral density plots of the principal components indicate an energy peak for the observed mode at about 40 days and an energy peak for the modeled mode at about 33 days.

The second type of pattern, represented by $VA2_O$ and $VA1_M$ (Fig. 15), represents a wave train arcing across the North Atlantic and Europe. The wave activity flux vectors indicate source regions over North America and the western Atlantic for both modes. These modes, and

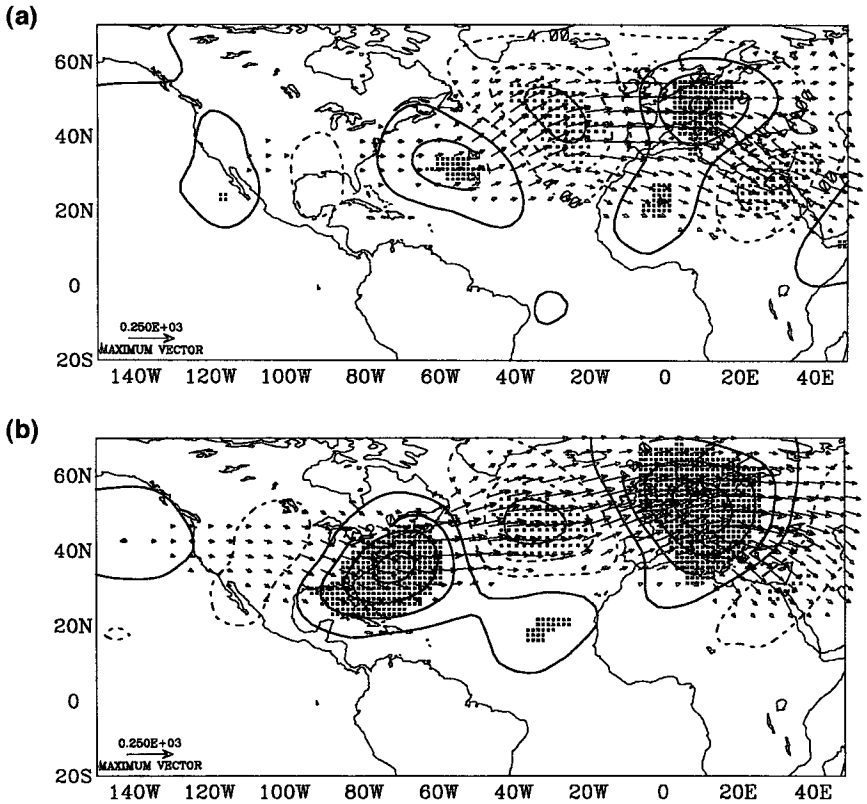

FIG. 15. The 200-mb streamfunction difference anomalies for (a) $VA2_O$ and (b) $VA1_M$. Contours at ± 4, ± 12, and $\pm 20 \times 10^6$ m^2 s^{-1} with positive (negative) values significant at the 99% level indicated by dark (light) shading. Negative contours are dashed. The corresponding horizontal wave activity fluxes are represented by the vectors (m^2 s^{-2}).

the modes in quadrature with them, represent 19% and 18% of the total intraseasonal variance in the V field in this region in the observations and model, respectively. Period spectral density plots of the principal components of the observed mode indicate a fairly flat spectrum within the 20–70-day range, while the modeled mode shows strong peaks at 30 and 45 days. The observed and modeled modes are quite similar except that the latter has greater variance over northern Europe, while the former has greater variance over North Africa and the Middle East. These differences are consistent with the difference in 200-mb U variability over North Africa (Fig. 2c).

The wave activity flux vectors shown in Fig. 15 have been superimposed on the 200-mb time-mean zonal wind in Fig. 16. As with the east–west-oriented wave trains over the Pacific, equatorward propagation of the wave train occurs in the exit region of the midlatitude jet. This occurs farther to the west in the observations than in the model, mirroring differences in the strength and extent of the observed and modeled jets. The meridional gradient of the zonal wind is much stronger in the model jet (Fig. 16b) than in the observations (Fig. 16a). This strong meridional gradient in the model appears to be acting as a waveguide that prevents equatorward energy propagation over western Europe and North Africa (Branstator 1983).

Unlike in the Pacific region, neither of the two primary observed patterns in the Atlantic V field has a significant signal in the tropical precipitation or velocity potential difference anomalies (not shown). Thus, it appears that in the Atlantic sector, where the primary modes of variability are not linked to tropical convection, the model simulates the observed modes well. This is consistent with the model intraseasonal variability being less deficient over the Atlantic and Europe than over the Pacific (Fig. 2c).

6. Discussion

For both the North Atlantic and North Pacific regions examined in this study, the primary observed intraseasonal modes that are related to tropical precipitation and upper-level divergence are poorly simulated by the NOGAPS model. This result is not surprising, given the model's (a) extremely weak MJO and (b) low tropical and extratropical intraseasonal variability in the regions where the observed MJO and its associated ex-

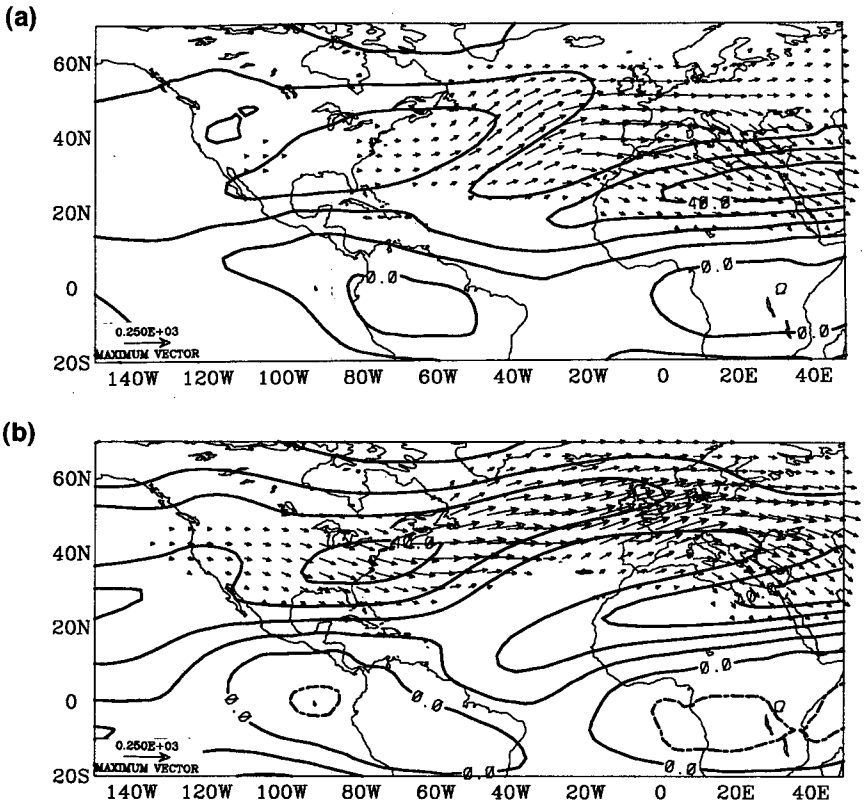

FIG. 16. The same wave activity flux vectors as in Fig. 15, superimposed upon the 200-mb U winter climatology for (a) observations and (b) model simulation. The contour interval is 10 m s^{-1}.

tratropical circulation anomalies are strong. In regions where the MJO exerts less influence, the model variability is closer to the observed levels.

On the other hand, the observed primary modes of variability that are not associated with tropical convection anomalies and that appear to be extratropically forced are well simulated by the model. The more subtle differences between the observed and modeled modes in this case may be related to model biases in the time-mean circulation. In particular, the tendency for the model jets to extend too far poleward and eastward over the Pacific and Atlantic (Fig. 1) appears to be related to these differences. Over the northern oceans, some of the model bias may be associated with a low number of blocking events compared with observations as computed using the criteria in Tibaldi and Molteni (1990). This undersimulation of blocking frequency results in stronger zonal flow in the time-mean fields of the model over the North Pacific and North Atlantic (Fig. 1). Although the model variability is deficient at timescales of weeks or longer, the model exhibits excessive variability at synoptic timescales (less than 6 days; not shown). This excess variance on synoptic timescales may be an indication that the model is not adequately simulating the transfer of energy from high to low frequencies commonly associated with blocking phenomena.

From the above results we may infer that an improved simulation of the MJO would also result in an improved simulation of the subtropical variability from Africa eastward to the central Pacific. Work is ongoing to improve the simulation of tropical convection, but improving the simulation of the MJO may not be so simple. It has been theorized that extratropical forcing may serve as a triggering mechanism for the MJO (Hsu et al. 1990; Murakami 1988). If this is the case, then it will be necessary to simulate properly the propagation of extratropical phenomena into the Tropics. This will, in turn, require a correct simulation of the background flow.

The above results should be evaluated with some specific caveats in mind. Recent studies have illustrated potential problems with using EOF and other eigenvector techniques to identify physically meaningful phenomena (e.g., Richman 1986; Bretherton et al. 1992). We have taken care to guard against these problems where possible. We have used rotated EOFs, which significantly reduces the potential for sampling errors (Richman 1986). While the rotated EOFS are sensitive to the number of modes retained for rotation,

all the modes shown here were affected little by the retention of one more or one less mode during rotation, and most were similar to the nonrotated modes. The sensitivity to domain size has also been tested and found to be minimal for most modes discussed in this study with domain changes of up to 20° latitude or longitude. Also, our composites at various time lags show spatially and temporally coherent signals, which gives us confidence that the modes shown here are physically meaningful.

The modes discussed in this study represent, in total, 37% and 28% of the observed U and V field intraseasonal variance, respectively, and 18% and 27% of the modeled U and V field intraseasonal variance, respectively, over the North Pacific. They represent 25% and 29% of the observed U and V field intraseasonal variance, respectively, and 9% and 37% of the modeled U and V field intraseasonal variance, respectively, over the North Atlantic. Because the observed and modeled EOFs are computed separately, comparison between the two is somewhat subjective. Procustus target rotation (Richman 1986) may be a useful extension of this study because it allows for a more quantitative evaluation of the percent variance of the observed modes that the model simulates by rotating the modeled EOFS toward the target of the observed EOFs.

The biases in the NOGAPS operational forecasts are much smaller than those in the 10-yr simulation, due to the operational model's higher resolution and the impact of data assimilation. However, many of the biases described in section 4 start to appear in the operational forecasts after only a few days, consistent with the results of Klinker and Sardeshmukh (1992), who found that the systematic 10-day forecast errors from ECMWF operational forecasts were qualitatively similar to the systematic errors in the initial tendencies. The impacts of these biases on operational forecasts, particularly those due to deficiencies in the simulation of tropical convection, are now being studied.

Acknowledgments. The 10-yr model simulation studied here was part of the AMIP project sponsored by the World Climate Research Programme and the Department of Energy and that is being conducted at the Naval Research Laboratory by Dr. Tim Hogan and Dr. Tom Rosmond. Mr. Jeff Hawkins aided in obtaining the satellite dataset. The ECMWF analyses were obtained through the National Center for Atmospheric Research. The authors would like to thank Dr. Patrick Harr for valuable discussions, and Mike Neith and John Kent for their work during the preliminary stages of this project. Support of the sponsor, Office of Naval Research, Program Element 0601153N, is gratefully acknowledged. Computing support was provided by the Department of Defense High-Performance Computing Program.

REFERENCES

Barnston, A. G., and R. E. Livezey, 1987: Classification, seasonality and persistence of low-frequency atmospheric circulation patterns. *Mon. Wea. Rev.*, **115,** 1083–1126.

Branstator, G., 1983: Horizontal energy propagation in a barotropic atmosphere with meridional and zonal structure. *J. Atmos. Sci.*, **40,** 1689–1708.

Bretherton, C. S., C. Smith, and J. M. Wallace, 1992: An intercomparison of methods for finding coupled patterns in climate data. *J. Climate,* **5,** 541–560.

Charney, J. G., 1969: A further note on large-scale motions in the tropics. *J. Atmos. Sci.,* **26,** 182–185.

Chen, T.-C., and J. C. Alpert, 1990: Systematic errors in the annual and intraseasonal variations of the planetary-scale divergent circulation in NMC medium-range forecasts. *Mon. Wea. Rev.,* **118,** 2607–2623.

Ferranti, L., T. Palmer, F. Molteni, and E. Klinker, 1990: Tropical–extratropical interaction associated with the 30–60 day oscillation and its impact on medium- and extended-range prediction. *J. Atmos. Sci.,* **47,** 2177–2199.

Held, I. M., 1982: Stationary and quasi-stationary eddies in the extratropical troposphere: Theory. *Large-Scale Dynamical Processes in the Atmosphere,* B. J. Hoskins and R. P. Pearce, Eds., Academic Press, 390 pp.

Hogan, T., and T. Rosmond, 1991: The description of the Navy Operational Global Atmospheric Prediction System's spectral forecast model. *Mon. Wea. Rev.,* **119,** 1786–1815.

——, and R. Brody, 1993: Sensitivity studies of the navy's global forecast model parameterizations and evaluation of improvements to NOGAPS. *Mon. Wea. Rev.,* **121,** 2373–2395.

Hoskins, B. J., I. N. James, and G. H. White, 1983: The shape, propagation and mean–flow interactions of large-scale weather systems. *J. Atmos. Sci.,* **40,** 1595–1612.

Hsu, H.-H., B. J. Hoskins, and F.-F. Jin, 1990: The 1985–1986 intraseasonal oscillations and the role of the extratropics. *J. Atmos. Sci.,* **47,** 823–839.

Kaylor, R. E., 1977: Filtering and decimation of digital time series. Tech. Note BN850, Institute for Physical Sciences and Technology, University of Maryland, College Park, MD, 42 pp.

Kiladis, G. N., and K. M. Weickmann, 1992a: Circulation anomalies associated with tropical convection during northern winter. *Mon. Wea. Rev.,* **120,** 1900–1923.

——, and ——, 1992b: Extratropical forcing of tropical convection during northern winter. *Mon. Wea. Rev.,* **120,** 1924–1938.

Klinker, E., and P. D. Sardeshmukh, 1992: The diagnosis of mechanical dissipation in the atmosphere from large-scale balance requirements. *J. Atmos. Sci.,* **49,** 608–627.

Knutson, T. R., and K. M. Weickmann, 1987: 30–60 day atmospheric oscillations: Composite life cycles of convection and circulation anomalies. *Mon. Wea. Rev.,* **115,** 1407–1436.

Kushnir, Y., and J. M. Wallace, 1989: Low-frequency variability in the Northern Hemisphere winter: Geographical distribution, structure, and time-scale dependence. *J. Atmos. Sci.,* **46,** 3122–3142.

Lau, K.-M., and H. Lim, 1984: On the dynamics of equatorial forcing of climate teleconnections. *J. Atmos. Sci.,* **41,** 161–176.

——, and K.-M. Lau, 1986: The structure and propagation of intraseasonal oscillations appearing in a GFDL general circulation model. *J. Atmos. Sci.,* **43,** 2023–2047.

——, and T. Phillips, 1986: Coherent fluctuations of extratropical geopotential height and tropical convection in intraseasonal time scales. *J. Atmos. Sci.,* **43,** 1164–1181.

——, and M. J. Nath, 1987: Frequency dependence of the structure and temporal development of wintertime tropospheric fluctuations—Comparison of a GCM simulation with observations. *Mon. Wea. Rev.,* **115,** 251–271.

——, and F. C. Chang, 1992: Tropical intraseasonal oscillations and extended range forecasts in the NMC operation model. *J. Climate,* **5,** 1365–1378.

Liebmann, B., and D. L. Hartmann, 1984: An observational study of tropical–midlatitude interaction on intraseasonal time scales during winter. *J. Atmos. Sci.,* **41,** 3333–3350.

Livezey, R. E., and K. C. Mo, 1987: Tropical–extratropical teleconnections during the Northern Hemisphere winter. Part II: Relationships between monthly mean Northern Hemisphere circulation patterns and proxies for tropical convection. *Mon. Wea. Rev.*, **115,** 3115–3132.

Madden, R., and P. Julian, 1972: Description of global-scale circulation cells in the tropics with a 40–50 day period. *J. Atmos. Sci.*, **29,** 1109–1123.

Mo, K. C., and V. E. Kousky, 1993: Further analysis of the relationship between circulation anomaly patterns and tropical convection. *J. Geophys. Res.*, **98,** 5103–5113.

Murakami, T., 1988: Intraseasonal atmospheric teleconnection patterns during the Northern Hemisphere winter. *J. Climate,* **1,** 117–131.

North, G. R., T. L. Bell, R. F. Cahalan, and F. J. Moeng, 1982: Sampling errors in the estimation of empirical orthogonal functions. *Mon. Wea. Rev.*, **110,** 699–709.

O'Lenic, E. A., and R. E. Livezey, 1988: Practical considerations in the use of rotated principal component analysis (RPCA) in diagnostic studies of upper-air height fields. *Mon. Wea. Rev.*, **116,** 1682–1689.

Park, C.-K., D. Straus, and K.-M. Lau, 1990: An evaluation of the structure of tropical intraseasonal oscillations in three general circulation models. *J. Meteor. Soc. Japan,* **68,** 403–417.

Plumb, R., 1985: On the three-dimensional propagation of stationary waves. *J. Atmos. Sci.*, **42,** 217–229.

Richman, M. B., 1986: Rotation of principal components. *J. Climatol.*, **6,** 293–335.

Sardeshmukh, P. D., and B. J. Hoskins, 1988: The generation of global rotational flow by steady idealized tropical divergence. *J. Atmos. Sci.*, **45,** 1228–1251.

——, and B. Liebmann, 1993: An assessment of low-frequency variability in the tropics as indicated by some proxies of tropical convection. *J. Climate,* **6,** 569–576.

Schubert, S., and C.-K. Park, 1991: Low-frequency intraseasonal tropical–extratropical interactions. *J. Atmos. Sci.*, **48,** 629–650.

——, M. Suarez, C.-K. Park, and S. Moorthi, 1993: GCM simulations of intraseasonal variability in the Pacific/North American region. *J. Atmos. Sci.*, **50,** 1991–2007.

Shapiro, L. J., and S. B. Goldenberg, 1993: Intraseasonal oscillations over the Atlantic. *J. Climate,* **6,** 677–699.

Simmons, A. J., J. M. Wallace, and G. W. Branstator, 1983: Barotropic wave propagation and instability, and atmospheric teleconnection patterns. *J. Atmos. Sci.*, **40,** 1363–1392.

Slingo, J. M., and R. A. Madden, 1991: Characteristics of the tropical intraseasonal oscillation in the NCAR community climate model. *Quart. J. Roy. Meteor. Soc.*, **117,** 1129–1169.

——, and Coauthors, 1995: Intraseasonal oscillations in 15 atmospheric general circulation models (results from an AMIP diagnostic subproject). World Climate Research Programme, WCRP-88, WMO/TD-No. 661.

Spencer, R., 1993: Global oceanic precipitation from the MSU during 1979–1991 and comparisons to other climatologies. *J. Climate,* **6,** 1301–1326.

Tibaldi, S., and F. Molteni, 1990: On the operational predictability of blocking. *Tellus,* **42A,** 343–365.

Tomas, R. A., and P. J. Webster, 1994: Horizontal and vertical structure of cross-equatorial wave propagation. *J. Atmos. Sci.*, **51,** 1417–1430.

Trenberth, K. E., and J. G. Olson, 1988: An evaluation and intercomparison of global analyses from the National Meteorological Center and the European Centre for Medium-Range Weather Forecasts. *Bull. Amer. Meteor. Soc.*, **69,** 1047–1057.

Wallace, J., and D. Gutzler, 1981: Teleconnections in the geopotential height field during the Northern Hemisphere winter. *Mon. Wea. Rev.*, **109,** 784–812.

Webster, P. J., and J. R. Holton, 1982: Cross-equatorial response to middle-latitude forcing in a zonally varying basic state. *J. Atmos. Sci.*, **39,** 722–733.

Zhang, C., and P. J. Webster, 1989: Effects of seasonal flows on equatorially trapped waves. *J. Atmos. Sci.*, **46,** 3632–3652.